The Astrophysical Journal, 993:47 (14pp), 2025 November 1 https://doi.org/10.3847/1538-4357/adfd50

Electronic Spectroscopy of C_{60}^+ and Its Analogs $C_{60}H_2O^+$, $C_{60}H^+$, $C_{60}D^+$, and $C_{60}Mg^+$

Lisa Ganner[1], Gabriel Schöpfer[1], Alexander Ebenbichler[2], Stefan Bergmeister[1], Milan Ončák[1], Helgi Rafn Hrodmarsson[3], and Elisabeth Gruber[1]
[1] Institute for Ion Physics and Applied Physics, University of Innsbruck Technikerstraße 25, 6020 Innsbruck, Austria
[2] Institute for Astro- and Particle Physics, University of Innsbruck Technikerstraße 25, 6020 Innsbruck, Austria
[3] CNRS, LISA UMR 7583, L'Université Paris-Est Créteil, Université Paris Cité, 61 avenue du Général de Gaulle, 94010 Créteil, France
Received 2025 February 25; revised 2025 July 31; accepted 2025 August 8; published 2025 October 23

Abstract

The fullerenes C_{60} and C_{70} have been detected in various interstellar environments, and the cation C_{60}^+ has been identified as a carrier of at least four of the diffuse interstellar bands (DIBs). Based on the presence of fullerenes in space, it is plausible that certain fullerene analogs are abundant in interstellar environments as well. In this context, we present the first electronic laboratory spectra of the analogs $C_{60}H_2O^+$, $C_{60}H^+$, $C_{60}D^+$, and $C_{60}Mg^+$. Furthermore, the electronic C_{60}^+ spectrum is remeasured and assignments of the observed transitions are proposed. In the spectrum of $C_{60}H_2O^+$, several distinct absorption features could be detected between 10,300 and 10,800 cm^{-1}, whereas the analogs $C_{60}H^+$, $C_{60}D^+$, and $C_{60}Mg^+$ show a broad absorption in the visible region between 17,000 and 25,000 cm^{-1}. None of the detected absorption features in these analogs of C_{60}^+ could be assigned to DIBs.

Unified Astronomy Thesaurus concepts: Electronic spectroscopy (2247); Diffuse interstellar bands (379); Fullerenes (2257); Interstellar molecules (849)

Materials only available in the online version of record: machine-readable tables

1. Introduction

The buckminsterfullerene C_{60} was discovered in 1985 by H. W. Kroto et al. (1985) and has since drawn substantial attention from the scientific community due to its remarkable structure and properties. Already at the time of its discovery, the authors suggested that C_{60} might be able to survive in space because of its extraordinary stability (H. W. Kroto et al. 1985); and, indeed, the C_{60} fullerene was later detected in several astronomical environments including planetary and reflection nebulae as well as young stellar objects (J. Cami et al. 2010; K. Sellgren et al. 2010; K. R. G. Roberts et al. 2012).

The presence of C_{60} in harsh astronomical environments is not entirely surprising, as its large dissociation energy (D. Muigg et al. 1996; K. Hansen & O. Echt 1997) compared to its small ionization energy (7.598 eV; H. R. Hrodmarsson et al. 2024), along with the capability to relax via recurrent fluorescence (O. Lacinbala et al. 2023), makes the molecule very photostable. Hence, the presence of the cationic buckminsterfullerene in space was early on considered plausible (H. W. Kroto & M. Jura 1992).

Recording the cation's laboratory gas-phase spectrum proved difficult, but early success was achieved with C_{60}^+ trapped in frozen noble gas matrices (J. Fulara et al. 1993), which led to the first claims that C_{60}^+ could be a good candidate as a carrier of the so-called diffuse interstellar bands (DIBs; B. H. Foing & P. Ehrenfreund 1994). The DIBs are a collection of over 600 diffuse absorption lines of varying spectral profiles and intensities that can differ along different sight lines from the optical blue to the near-IR (H. Fan et al. 2019). Eventually, helium-tagging messenger spectroscopy yielded the near-IR laboratory gas-phase spectrum of C_{60}^+, resulting in the identification of C_{60}^+ as the carrier of at first two (E. K. Campbell et al. 2015) and later four DIBs (along with a tentative fifth; G. A. H. Walker et al. 2015, 2016; E. K. Campbell et al. 2016b; H. Linnartz et al. 2020; T. P. Nie et al. 2022). Single helium atoms were attached to the C_{60}^+ ions in a cryogenic ion trap, and the dissociation of the helium tag from the C_{60}^+ ion upon photon absorption was monitored (E. K. Campbell et al. 2015). As the bond between the ion and the He atom is weak, the attachment of the He atom is generally considered to induce only a small shift in the absorption wavelength (E. K. Campbell et al. 2015; M. Kuhn et al. 2016). In the case of C_{60}^+, the first 32 attached He atoms form a solid shell above the 32 facets of the fullerene, and a linear redshift of the two major near-IR absorption bands by ≈0.07 nm per He atom is observed (E. K. Campbell et al. 2016a; M. Kuhn et al. 2016; S. Albertini et al. 2021).

We have recently developed a helium-tagging messenger spectroscopy setup which uses multiply-charged superfluid helium nanodroplets (HNDs) to form helium-tagged ions, providing an alternative to the cryogenic trap method mentioned above (S. Bergmeister et al. 2023). In this setup, multiply-charged HNDs are produced by expanding pressurized, cooled helium into a vacuum, followed by electron-impact ionization (F. Laimer et al. 2019). The HNDs are then doped with the molecules of interest, which become ionized within the charged helium matrix. The helium-tagged ions are eventually created in a top-down approach by shrinking the doped HNDs upon collision with room-temperature helium gas. After mass-to-charge selection in a quadrupole mass filter, the ions are investigated under laser irradiation. A detailed description of the measurement principle is given in Appendix A.

With this method, we have reproduced the electronic C_{60}^+ absorption spectrum in the near-IR. In addition to the five well-known absorption bands, we have recorded many other weaker absorption bands in the near-IR, which were also earlier detected by E. K. Campbell et al. (2016b). In this contribution, we provide assignments to the spectrum based on the

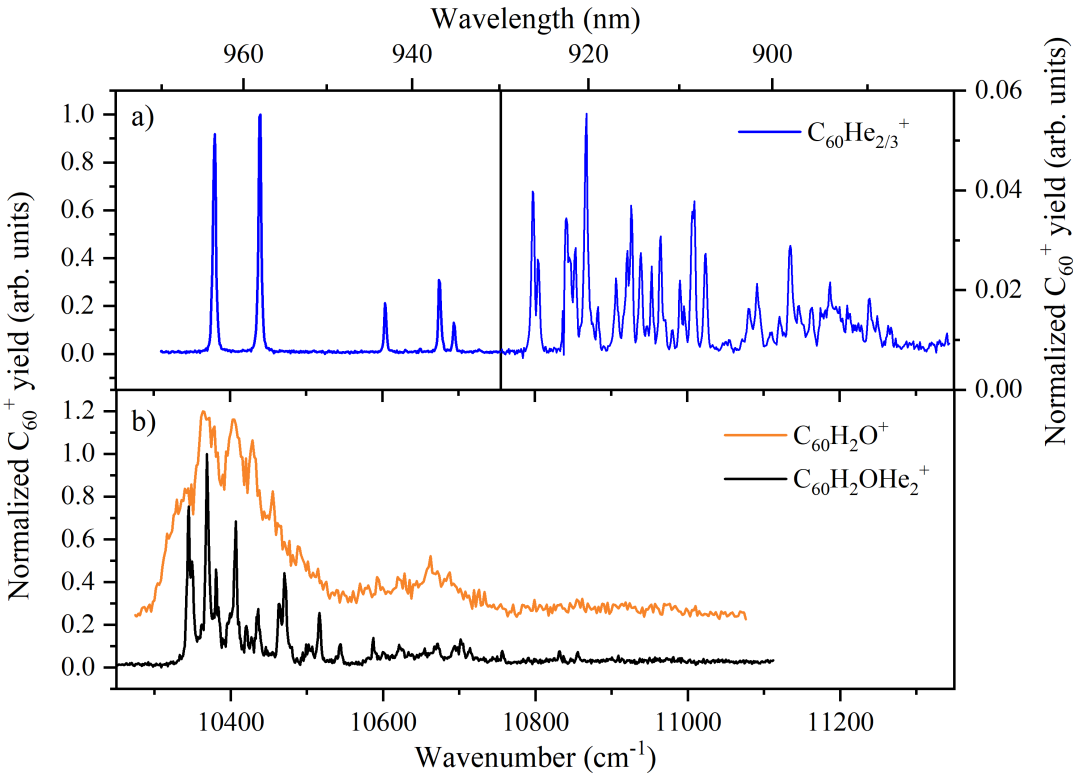

Figure 1. (a) Absorption spectra of $C_{60}He_{2/3}^+$ and (b) $C_{60}H_2O^+$ (orange) and $C_{60}H_2OHe_2^+$ (black) obtained by recording the laser-frequency-dependent C_{60}^+ yield. For the spectrum shown in (a), several recorded spectra of $C_{60}He_2^+$ and $C_{60}He_3^+$ were combined and shifted by -2×0.07 and -3×0.07 nm to account for the attached He atoms, respectively.

theoretical formalism of A. O. Lykhin et al. (2018) and recreate the spectrum with the PGOPHER software (C. M. Western 2017).

In addition, we have investigated the effect of single water molecule attachment to C_{60}^+. Water has been found to be abundant in many astrophysical environments (E. F. van Dishoeck et al. 2013), rendering the formation of $C_{60}H_2O^+$ possible. Previously, spectroscopy of endohedral $H_2O@C_{60}^+$, where a water molecule is encapsulated inside a C_{60}^+ ion, was studied (J. Rademacher et al. 2023), whereas here we investigate exohedral cationic C_{60}-water complexes in the near-IR.

From observations of C_{60} in multiple environments, it is also likely that the spectral features of fullerenes in space are contaminated by other fullerene analogs (A. C. Brieva et al. 2016), and previous works have suggested that hydrogenated C_{60} might be present in circumstellar envelopes (J. J. Díaz-Luis et al. 2016; Y. Zhang et al. 2017). Dedicated modeling works suggest that $C_{60}H^+$ should be the most abundant hydrogenated fullerene species in the diffuse interstellar medium (ISM; H. W. Kroto & M. Jura 1992; D. Abbink et al. 2024). In this contribution, we report an experimental gas-phase spectrum of $C_{60}H^+$ in the visible range. Whereas, to the best of our knowledge, the electronic spectrum of $C_{60}H^+$ has not been thoroughly studied (F.-X. Hardy 2016), IR spectra of $C_{60}H^+$ have been reported by the group of J. Oomens (J. Palotás et al. 2020; L. Finazzi et al. 2024). The measurements from J. Palotás et al. (2020) coincide with observational data from two planetary nebulae indicating that $C_{60}H^+$ might indeed be abundant in the ISM. Concerning the electronic transitions of $C_{60}H^+$, it was suggested that the hydrogen atom tunnels between the potential wells on the C_{60} cage, resulting in broadening of electronic absorption features (H. W. Kroto & M. Jura 1992). As tunneling is supposed to be less pronounced for heavier atoms such as deuterium, we also provide the electronic spectrum of $C_{60}D^+$.

Besides hydrogenated C_{60}^+, it has been suggested that cationic C_{60}-metal complexes are present in space and represent potential DIB carriers (H. W. Kroto & M. Jura 1992; G.-L. Hou et al. 2023) as metals like Na, K, Mg, Ca, Al, and Fe are abundant in space (M. Asplund et al. 2021). G.-L. Hou et al. (2023) have recently proposed $(C_{60}\text{-metal})^+$ complexes as possible carriers of unidentified IR emission bands. In this contribution, we present the first experimental electronic spectrum of exohedral $C_{60}Mg^+$ and discuss its suitability as a carrier of DIBs. Several cationic molecules containing Mg have recently been identified in the carbon-rich star IRC +10216, demonstrating the presence of cationic metal-bearing complexes in space (J. Cernicharo et al. 2023). Regarding $C_{60}Mg^+$, G.-L. Hou et al. (2023) estimated a lower interstellar formation rate limit of $3.16 \times 10^{-11}\,s^{-1}$ per C_{60}^+. The thermal dissociation rate of $C_{60}Mg^+$ at an interstellar temperature of 300 K was determined to be $2 \times 10^{-3}\,s^{-1}$, thus greatly exceeding the formation rate (G.-L. Hou et al. 2023). However, at a lower ISM temperature of 50 K, the thermal dissociation approaches zero, making the presence of $C_{60}Mg^+$ possible (G.-L. Hou et al. 2023).

2. Results and Discussion

In Figure 1, the absorption spectrum of $C_{60}He_{2/3}^+$ is presented. Helium-tagged C_{60}^+ ions were formed upon the shrinking of HNDs containing C_{60}^+ ions, after which $C_{60}He_2^+$ or $C_{60}He_3^+$ ions were selected with a quadrupole mass filter. To obtain the absorption spectrum, the selected $C_{60}He_2^+$ or

$C_{60}He_3^+$ ions were irradiated with a tunable Nd:YAG-pumped OPO laser, and the yield of the photofragment C_{60}^+ was recorded as a function of the laser frequency. Further information on the experimental methods and the signal normalization is given in Appendix A. For the spectrum shown in Figure 1(a), several recorded spectra of $C_{60}He_2^+$ and $C_{60}He_3^+$ were combined. As mentioned above, it was shown that the two strongest absorption bands of helium-tagged C_{60}^+ redshift linearly by 0.07 nm per helium atom (E. K. Campbell et al. 2016a; M. Kuhn et al. 2016; S. Albertini et al. 2021). The effect of the first helium atom is not yet known; however, extrapolation to zero attached helium atoms yields an estimate of the bare C_{60}^+ band positions. Accordingly, the recorded spectra were extrapolated to bare C_{60}^+ by employing a wavelength shift of 0.07 nm ($\approx$0.8 cm^{-1} in the studied wavelength range) per attached helium atom. The five strongest peaks in the left side of panel (a) are already well known and have been assigned to DIBs (E. K. Campbell et al. 2015, 2016b; G. A. H. Walker et al. 2015, 2016; H. Linnartz et al. 2020; T. P. Nie et al. 2022). Parts of the weaker bands in the right side of panel (a) have also already been recorded by E. K. Campbell et al. (2016b), however their low intensity has hindered astronomical detection up to now (E. K. Campbell et al. 2016b). The central band positions, FWHMs, and relative intensities of the measured bands are given in Table 1 along with data from E. K. Campbell et al. (2016b), E. K. Campbell et al. (2016a), and E. K. Campbell & J. P. Maier (2018), showing a close match between them.

Helium is suggested to have a minor effect, whereas H_2O will more strongly affect the C_{60}^+ spectrum. In panel (b) of Figure 1, the effect of water attachment on the spectrum of C_{60}^+ is shown. The orange line corresponds to the spectrum of $C_{60}H_2O^+$ and the black line corresponds to the spectrum of $C_{60}H_2OHe_2^+$. Both spectra in Figure 1(b) were obtained by recording the yield of the bare C_{60}^+ ion as the absorption of a photon in the studied energy range leads to the evaporation of the attached helium atoms as well as the attached H_2O molecule. Due to the higher temperature, the spectrum of $C_{60}H_2O^+$ without helium attached is rather broad, whereas the attachment of helium to the $C_{60}H_2O^+$ ion implies a lower temperature ($\approx$4–5 K), narrowing the spectral features. Furthermore, we also recorded the absorption spectra of $C_{60}(H_2O)_j^+$ ($j = 2$–4) in the same spectral range, which are presented in Figure C1 in Appendix C. The formation of the (helium-tagged) cationic C_{60}-water species in our setup is explained in Appendix A.

The positions and the relative cross sections of the $C_{60}H_2OHe_2^+$ bands between 10,300 and 10,550 cm^{-1} were determined with Lorentzian fits and are given in Table 2. In the electronic spectrum of endohedral $H_2O@C_{60}^+$ reported by J. Rademacher et al. (2023), the absorption bands lie in the range of 10,400–10,700 cm^{-1}, and the lowest excitation energies they observed were at 10,429 cm^{-1} for ortho-$H_2O@C_{60}^+$ and 10,438 cm^{-1} for para-$H_2O@C_{60}^+$, respectively (J. Rademacher et al. 2023). Compared to these, the absorption lines of exohedral $C_{60}H_2O^+$ presented here are redshifted.

As the $C_{60}H_2O^+$ compounds dissociate upon photon absorption in this energy range, their spectroscopic detection is unlikely. Nevertheless, we visually compared the narrow transitions of $C_{60}H_2OHe_2^+$ to astronomical spectra from the Ultraviolet and Visual Echelle Spectrograph (UVES) of the European Southern Observatory with sight lines toward HD 185859, HD 63804, HD 183143, HD 167971, HD 75860, HD 186841, HD 186745, HD 169454, HD 167838, HD 170938, and HD 112272. All of those sight lines show strong absorptions of C_{60}^+ at 963.21 and 957.7 nm, however no signs of $C_{60}H_2O^+$ were found in those interstellar spectra.

Compared to the spectrum of C_{60}^+ with weakly bound He atoms attached, the attachment of water results in a spectrum with a greater number of absorption bands of similar intensity. However, the similarity of the spectra of helium-tagged C_{60}^+ and $C_{60}H_2OHe_2^+$ indicates that, in contrast to the stronger bound complexes ($C_{60}H^+$, $C_{60}D^+$, $C_{60}Mg^+$) discussed below, which do not exhibit narrow absorption features in the near-IR range between 14,100 and 10,000 cm^{-1}, the C_{60}-water ion complex can spectroscopically still be viewed as a C_{60}^+ perturbed by the attached water. For a better understanding, we employed quantum-chemical calculations. The calculated structure and binding energy for $C_{60}H_2O^+$ are given in Figure 2. The water molecule interacts with the C_{60}^+ through the oxygen atom, with a C···O distance of 2.82 Å. According to our calculations, the water molecule is bound by 0.11 eV, which is roughly consistent with the value of 0.18 eV from prior theoretical studies (S. Denifl et al. 2009; J. Hernández-Rojas et al. 2010). The differences can be traced to a different density functional used here (see Appendix D). As the ionization energy of C_{60} (7.598 eV; H. R. Hrodmarsson et al. 2024) is lower than that of H_2O ($\approx$12.6 eV; R. H. Page et al. 1988), the charge supposedly stays on the C_{60}, which agrees with the role of H_2O being only a perturbance. According to our calculations, the H_2O attachment leads to splitting of the degenerate bright $^2E_{1g}$ state of C_{60}^+ into $^2A'$ and $^2A''$ states with calculated excitation energy in the fixed ground-state structure at 9620 and 12,228 cm^{-1} (TD-BMK/6-31+G*//BP86-D3/def2SVP). The shift compared to the excitation in C_{60}^+ (10,705 cm^{-1}) is too large compared to the shift in the experiment. However, in the experiment the 0–0 transition is measured. In order to calculate this transition, the optimized geometry in the electronically excited state is required as well as the respective vibrational frequencies. Unfortunately, we have not succeeded in optimizing the geometry in the excited state of $C_{60}H_2O^+$ due to convergence issues. Therefore, we calculate vertical transitions in the minimum geometry of the ground state; see Figure E1 in Appendix E. This approach provides only the first approximation to the 0–0 transition.

In Figure 3, the experimental C_{60}^+ spectrum from Figure 1 is compared to a model constructed in PGOPHER (C. M. Western 2017), which is roughly based on the theoretical formalism of C_{60}^+ electronic excitation developed by A. O. Lykhin et al. (2018), allowing us to provide some tentative assignments to the peaks. The assignments are listed along with the band characteristics in Table 1. According to A. O. Lykhin et al. (2018), the electronic excitation is from a non-Franck–Condon region of the ground electronic state to two components of the lowest $^2E_{1g}$ state split by a pseudo-Jahn–Teller (JT) effect into ^2A_g and ^2B_g vibrational progressions of C_{2h} symmetry. The ^2A_g and ^2B_g manifolds have here been approximated with anharmonic oscillators described by the formula $\tilde{E} = \tilde{\nu}_0 + \omega_e(v' + 0.5) - \omega_e x_e(v' + 0.5)^2 + \omega_e y_e(v' + 0.5)^3$, where $\tilde{\nu}_0$, ω_e, $\omega_e x_e$, and $\omega_e y_e$ are the fitted vibrational constants (presented in Table 3), and v' are the vibrational quantum numbers. The recorded spectrum allows us to assign the components $v' = 0$–4 for both ^2A_g and ^2B_g manifolds, but these are insufficient to account for all of the spectral structures observed in Figure 3.

Table 1
Central Wavenumber $\tilde{\nu}_c$, Wavelength $\tilde{\lambda}_c$ in Air, FWHM, and Relative Cross Section σ_{rel} of the $C_{60}He_{2/3}^+$ Absorption Bands in Figure 1(a) along with Their Tentative Assignments

This Work[a]						E. K. Campbell et al. (2016a, 2016b), E. K. Campbell & J. P. Maier (2018)[b]		
Assignment	$\tilde{\nu}_c$ (cm^{-1})	$\tilde{\lambda}_c$ (nm)	FWHM (cm^{-1})	FWHM (nm)	σ_{rel}[c]	$\tilde{\lambda}_c$ (nm)	FWHM (nm)	σ_{rel}[c]
^2B_g ($v' = 0$)	10,379.49(4)	963.17	4.7	0.44	0.95	963.21(2)[d,e]	0.22(2)[f]	0.84[g]
^2A_g ($v' = 0$)	10,439.16(3)	957.67	4.3	0.39	1	957.70(2)[d,e]	0.25(2)[f]	1.00[g]
^2B_g ($v' = 1$)	10,603.84(8)	942.80	3.1	0.27	0.19	942.78(2)[d]	0.24(1)[f]	0.17[g]
$^2E_?$ ($v' = 0$)	10,630.7(17)	940.42	4	0.36	0.02	…	…	…
$^2E_?$ ($v' = 0$)	10,649.7(12)	938.74	4	0.35	0.02	…	…	…
^2A_g ($v' = 1$)	10,675.12(6)	936.50	3.4	0.30	0.33	936.52(2)[d]	0.24(1)[f]	0.26[g]
$^2A_{1g}$ ($v' = 0$)	10,694.28(14)	934.83	3.2	0.28	0.12	934.84(2)[d]	0.23(2)[f]	0.09[g]
$^2E_?$ ($v' = 0$)	10,726.9(15)	931.98	5.0	0.43	0.02	…	…	…
^2B_g ($v' = 2$)	10,797.5(1)	925.89	4.0	0.34	0.04	925.89(2)[f]	0.27[f]	0.03[f]
$^2E_?$ ($v' = 0$)	10,804.7(1)	925.28	3.2	0.28	0.02	925.31(2)[f]	0.23[f]	0.01[f]
$^2E_?$ ($v' = 0$)	10,841.2(1)	922.16	4.1	0.35	0.03	922.2(2)[f]	0.27[f]	0.02[f]
…	10,846.2(2)	921.73	5.1	0.43	0.02	…	…	…
$^2E_?$ ($v' = 1$)	10,853.0(1)	921.16	3.2	0.28	0.02	921.19(2)[f]	0.21[f]	0.02[f]
^2A_g ($v' = 2$)	10,867.95(5)	919.95	4.8	0.41	0.07	919.98(2)[f]	0.37[f]	0.03[f]
$^2E_?$ ($v' = 1$)	10,882.6(2)	918.65	3.8	0.32	0.01	…	…	…
$^2E_?$ ($v' = 0$)	10,906.6(4)	916.63	4.7	0.40	0.02	…	…	…
…	10,921.1(1)	915.41	3.9	0.32	0.02	915.44(2)[f]	0.19[f]	0.01[f]
$^2A_{1g}$ ($v' = 1$)?	10,926.9(1)	914.93	3.4	0.28	0.03	914.96(2)[f]	0.26[f]	0.02[f]
$^2A_{1g}$ ($v' = 1$)?	10,939.1(1)	913.91	4.3	0.36	0.03	913.95(2)[f]	0.2[f]	0.01[f]
$^2E_?$ ($v' = 1$)	10,953.4(1)	912.72	3.1	0.26	0.01	912.73(2)[f]	0.3[f]	0.01[f]
^2B_g ($v' = 3$)	10,964.9(1)	911.76	3.7	0.31	0.03	911.80(2)[f]	0.23[f]	0.02[f]
…	10,990.6(1)	909.62	3.3	0.28	0.01	909.64(2)[f]	0.22[f]	0.01[f]
…	10,996.2(3)	909.16	3.0	0.25	0.01	…	…	…
$^2E_?$ ($v' = 1$)	11,006.3(1)	908.33	3.5	0.29	0.03	908.36(2)[f]	0.25[f]	0.01[f]
$^2E_?$ ($v' = 2$)	11,009.6(1)	908.05	3.0	0.25	0.02	908.07(2)[f]	0.25[f]	0.01[f]
^2A_g ($v' = 3$)	11,023.9(1)	906.87	4.1	0.34	0.01	…	…	…
$^2E_?$ ($v' = 2$)	11,080.8(4)	902.22	6.8	0.55	0.02	…	…	…
$^2E_?$ ($v' = 1$)	11,092.2(2)	901.29	7.3	0.60	0.03	…	…	…
$^2E_?$ ($v' = 3$)	11,109.8(7)	899.87	6.3	0.51	0.01	…	…	…
^2B_g ($v' = 4$)	11,121.4(4)	898.93	4.7	0.38	0.01	…	…	…
$^2A_{1g}$ ($v' = 2$)	11,135.4(1)	897.80	6.1	0.50	0.04	…	…	…
^2A_g ($v' = 4$)[h] and $^2E_?$ ($v' = 2$)	11,146.7(6)	896.88	6.8	0.55	0.01	…	…	…
$^2E_?$ ($v' = 1$)	11,163.2(3)	895.56	7.1	0.57	0.02	…	…	…

Notes. All assignments assume the lower state to be the $^2A_{1u}(v' = 0)$ ground state (see Figure 3). The spectrum already includes a shift of 0.07 nm (≈0.8 cm^{-1}) per attached helium atom. The two 0–0 transitions have been fitted with a Voigt function for a better fit and the other peaks have been fitted with Lorentzian functions. On the right side of the table, data from E. K. Campbell et al. (2016a, 2016b) and E. K. Campbell & J. P. Maier (2018) are presented for comparison. Note that we also employed a shift of −0.07 nm to the $\tilde{\lambda}_c$ values from E. K. Campbell et al. (2016a, 2016b) to make them better comparable to our data.

[a] The uncertainty of the central position is the standard error from the fit, however we estimate that for most values the systematic error is bigger. We estimate a systematic uncertainty in the employed He shift of about ±0.01 nm/±0.1 cm^{-1} per He atom, resulting in a total systematic uncertainty of up to about ±0.03 nm/±0.3 cm^{-1}. The FWHM values represent upper limits to the natural line width due to several broadening mechanisms: a laser line width of up to 3 cm^{-1}, different isomers (see [d]), saturation, overlap of multiple bands that are not resolved, etc. The values of the relative cross sections are also subject to several systematic uncertainties (ion–laser overlap, saturation, etc.), thus the values should be regarded as approximate. In particular, the two major bands might experience saturation, which would explain the higher relative cross sections in our data compared to the literature values.

[b] The FWHM values represent upper limits if no uncertainty is listed. The uncertainty of the relative cross section is reported as about 20% in E. K. Campbell et al. (2016b), and greater accuracy is assumed for the relative cross section data from E. K. Campbell & J. P. Maier (2018).

[c] The cross sections are relative to the strongest band at 957.67 nm.

[d] E. K. Campbell et al. (2016a).

[e] Most recent data from E. K. Campbell & J. P. Maier (2018) have revealed an asymmetry in the 957.7 and 963.2 nm bands of $C_{60}He^+$ which is likely caused by the difference in the binding energy of helium to the hexagonal and pentagonal faces of C_{60}. Fitting each transition with a double Lorentzian function yielded central wavelengths of 957.74 and 957.83 nm as well as 963.26 nm and 963.43 nm, respectively. Each band was fitted with a FWHM of 0.14 nm, which indicates that the C_{60}^+ bands might be narrower than the 0.22–0.25 nm expected before.

[f] E. K. Campbell et al. (2016b).

[g] E. K. Campbell & J. P. Maier (2018).

[h] We assume that this rather broad peak contains unresolved contributions from both a $^2A_g(v' = 4)$ and a $^2E_?(v' = 2)$ state.

The $^2E_{1g}$ state is not the only electronically excited state expected in proximity to the spectral region recorded. Recently, M. Kappe et al. (2023) recorded an electronic spectrum of C_{60}^+ which evidenced the first two excited states of C_{60}^+, namely $^2E_{2u}$ and $^2E_{1u}$, that are supposedly dark states with zero computed oscillator strengths. These have since also

Table 2
Central Position $\tilde{\nu}_c$, FWHM, and Relative Cross Section σ_{rel} of the $C_{60}H_2OHe_2^+$ Absorption Bands

$\tilde{\nu}_c$ (cm^{-1})	FWHM (cm^{-1})	σ_{rel}[a]	$\tilde{\nu}_c$ (cm^{-1})	FWHM (cm^{-1})	σ_{rel}[a]
10,344.6(1)	3.5	0.6	10,420.6(3)	3.4	0.1
10,349.6(1)	4.3	0.4	10,427.4(6)	2.8	0.04
10,361.3(6)	2.8	0.05	10,435.7(3)	6.2	0.3
10,369.2(1)	4.6	1.0	10,463.7(2)	3.8	0.2
10,381.3(2)	5.8	0.5	10,471.1(1)	5.2	0.5
10,398.9(7)	10.0	0.4	10,516.4(2)	4.2	0.2
10,406.6(1)	4.2	0.6	10,543.8(4)	3.6	0.08

Notes. The band positions and relative cross sections were determined with Lorentzian fits to the spectrum displayed in Figure 1(b). No wavelength shift was employed here due to the lack of data on the effect of helium attachment on the $C_{60}H_2O^+$ spectrum. The uncertainties for the central position are the standard errors of the fit. The FWHM values should be regarded as upper limits and the relative cross sections as approximate values for the same reasons stated in Table 1.
[a] The cross sections are relative to the strongest band at 10,369.2 cm^{-1}.

been assigned in the threshold photoelectron spectrum (TPES) of C_{60} by H. R. Hrodmarsson et al. (2024). It appears that, as in polycyclic aromatic hydrocarbons (H. Álvaro Galué et al. 2016), excited states of C_{60}^+ might experience intensity borrowing by means of Herzberg–Teller effects as the vibrationally active low-lying excited states mix and "soften" the ground state. Hence, many more electronically excited states could in fact be visible in the optical spectrum which are a priori predicted to be dark.

Shown in Table 4 are results of two sets of calculations (at the TD-BMK/6-31+G* and TD-BHandHLYP/6-31+G* levels) of both the energies and the oscillator strengths of the excited states of C_{60}^+. The results depend strongly on the method used and show that the order of appearance of the excited states is somewhat uncertain. Where available, we also include comparisons with the work of A. O. Lykhin et al. (2018), whose calculations were performed at the TD-B3LYP/def2-TZVP level of theory. The differences between the results of the three methods can be interpreted as an estimate of the error associated with the calculations.

Table 4 shows that there are multiple other doubly degenerate E states accessible in this region in addition to two A states. If we assume that the states behave similarly to the $^2E_{1g}$ state, i.e., being split into two components that can be approximated with an anharmonic oscillator, these can be simulated to convincingly replicate the experimental spectrum (Figure 3). As there is one state starting at 10,694 cm^{-1} with more than twice the intensity of the cluster of peaks starting around 10,800 cm^{-1}, we make a tentative assignment to the $^2A_{1g}$ state based on it appearing to be a nondegenerate state, i.e., not an E state. If it was a doubly degenerate state, one would expect two $v' = 0$ peaks of similar intensity as with the ^2A_g and ^2B_g components.

As described in A. O. Lykhin et al. (2018), the proximity of the first two excited states to the ground state induces JT effects that distort the geometry of the ground state, effectively "softening" it and making various other electronic transitions allowed. This effect could likewise lift the degeneracy of the other excited E states and, in addition to the Herzberg–Teller effect of intensity borrowing, allow transitions from the $^2A_{1u}$ ground state thanks to being mixed with the low-lying $^2E_{2u}$ and $^2E_{1u}$ states.

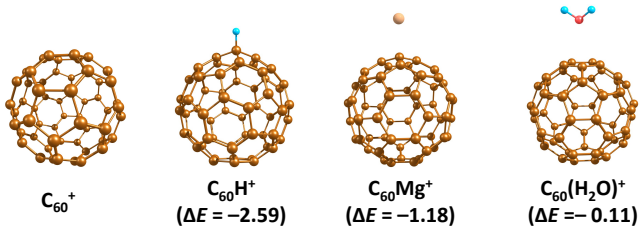

Figure 2. Structures of the fullerene cation C_{60}^+ along with the substituted fullerene cation with H, Mg, and H_2O as calculated at the BP86-D3/aug-cc-pVDZ level. ΔE corresponds to the zero-point-corrected electronic energies of formation in electronvolts (eV) for the reaction $C_{60}^+ + M \rightarrow C_{60}M^+$, M = {H, Mg, H_2O}.

We also compare the modeled spectrum with that of the TPES of the second photoelectron band (H. R. Hrodmarsson et al. 2024). This is achieved by increasing the temperature and line-broadening coefficients in PGOPHER (Figure 4). The energy of the modeled spectrum (or $\tilde{\nu}_0$) in comparison to the TPES was calculated as the sum of the ionization energy and the energetic content of the first C_{60}^+ DIB (9632 Å) transition. The resulting broadened spectrum replicates the principal features of the TPES well. Additionally, by coadding the scaled spectra to the red portion of the spectrum, we see that by reducing the energy by the amount carried in the Raman-active bands $h_g(2)$ (437 cm^{-1}, 54 meV) and $h_g(5)$ (1099 cm^{-1}, 136 meV) (N. Manini et al. 2001), they perfectly align with the hot bands of the TPES. This is a sensible conclusion as the C_{60} molecules in the original experiment of H. R. Hrodmarsson et al. (2020) were sublimated at 600 °C before being seeded in a supersonic beam. The carrier gas Ar was not an efficient means for vibrational cooling, and thus the recorded TPES exhibited several hot bands to the red. Additional structure is present in the TPES above 9 eV that remains unassigned, but this could be due to higher electronically excited states or from other JT-active splittings in the excited states that may manifest as more complex vibrational structures than that of an anharmonic oscillator.

In Figure 5, the helium-tagging spectra of the more strongly bound $C_{60}H^+$, $C_{60}D^+$, and $C_{60}Mg^+$ complexes in the visible range are shown. Besides the presented spectra, the near-IR range between 10,000 and 14,100 cm^{-1} has been measured for $C_{60}H^+$, $C_{60}D^+$ and $C_{60}Mg^+$; however, none of these spectra revealed any pronounced absorption features. The absorption spectra were obtained by measuring the yield of the fragment —$C_{60}H^+$, $C_{60}D^+$, $C_{60}Mg^+$—emerging from the photoabsorption by the precursor—$C_{60}HHe_3^+$, $C_{60}DHe_3^+$, $C_{60}MgHe_2^+$—which was selected with the quadrupole mass filter, respectively. The formation of helium-tagged $C_{60}H^+$, $C_{60}D^+$, and $C_{60}Mg^+$ ions is explained in more detail in Appendix A. For comparison, we also display the spectrum of $C_{60}He_3^+$ in panel (a) of the figure. Along with the experimental spectra, we present modeled spectra of C_{60}^+, $C_{60}H^+$, and $C_{60}Mg^+$ at the TD-BMK/6-31+G*//BP86-D3/def2SVP level of theory (see Appendix D). The electronic spectra are shown in Figure 5, and the underlying structures are given in Figure 2. We also calculated electronic excitations in the high-symmetry structure of a neutral C_{60} molecule, however there were no allowed transitions in the energy range under concern. These transitions become allowed only through symmetry breaking due to

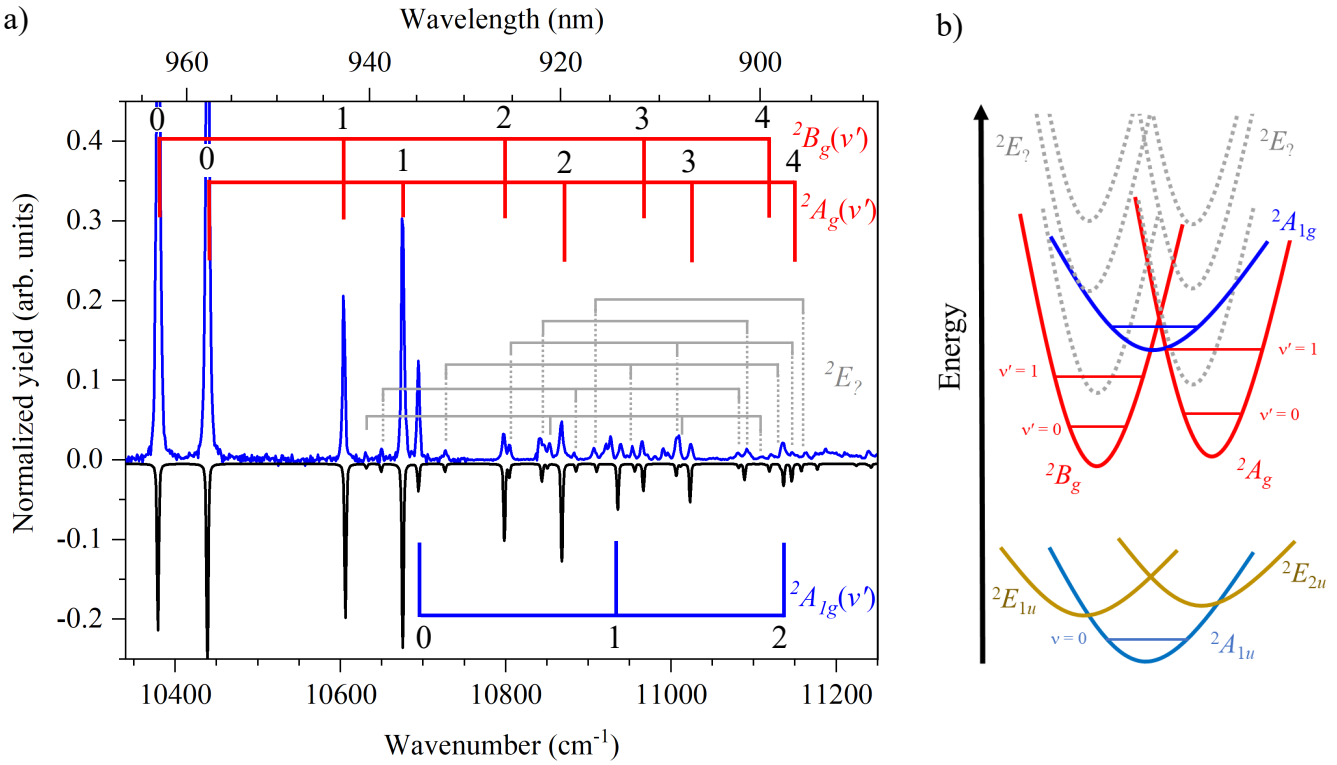

Figure 3. (a) Experimental C_{60}^+ spectrum (blue) and the PGOPHER model (black) with assignments. The red-colored assignment bars correspond to the ^2A_g and ^2B_g vibrational progressions of the JT-split $^2E_{1g}$ state. The blue-colored assignment bar corresponds to the singly degenerate $^2A_{1g}$ state. The pale gray assignment bars correspond to more tentative assignments to other ^2E states that may also be split from JT distortions. (b) Simplified energy level diagram of the C_{60}^+ cation in part based on the theoretical work of A. O. Lykhin et al. (2018).

Table 3
Spectroscopic Constants Used to Replicate the Experimental $C_{60}He_{2/3}^+$ Spectrum in the PGOPHER Program

Constant	X ($^2A_{1u}$)	$^2E_{1g}$ (^2B_g)	$^2E_{1g}$ (^2A_g)	$^2A_{1g}$	$^2E_?$	$^2E_?$	$^2E_?$	$^2E_?$	$^2E_?$	$^2E_?$
$\tilde{\nu}_0$	0	10,362.2	10,407.1	10,679	10,606	10,621	10,699	10,796	10,833	10,890
ω_e	250	268.3	285	262	280	277	281	264	250	257
$\omega_e x_e$	20	23.8	26	14	30	20	26	31	0	0
$\omega_e y_e$	0.3	1.58	0.95	0	0	0	0	0	0	0

Note. All constants are given in cm^{-1}.

vibrations, which would be computationally too expensive to quantify.

When evaluating the photofragment spectra of $C_{60}H^+$ and $C_{60}D^+$, care had to be taken as the selected *m/z* ratios of the precursors $C_{60}HHe_3^+$ and $C_{60}DHe_3^+$ coincide with the *m/z* ratio of the $^{12}C_{59}$ $^{13}CHe_3^+$ and $^{12}C_{58}{}^{13}C_2He_3^+$ isotopes, respectively. Hence, also the photofragment peaks at the *m/z* of $C_{60}H^+$ and $C_{60}D^+$ will be affected by the $^{12}C_{59}$ $^{13}C^+$ and $^{12}C_{58}$ $^{13}C_2^+$ isotopes. In the displayed spectra in panels (c) and (d) of Figure 5, the estimated contribution of C_{60}^+ isotopes in the photofragment yield has already been subtracted. Further information on the evaluation of the $C_{60}H^+$ and $C_{60}D^+$ absorption spectra is given in Appendix B. The measurements of $C_{60}Mg^+$ showed that the selected precursor $C_{60}MgHe_2^+$ did not only dissociate into $C_{60}Mg^+$ but a small fraction would also dissociate into C_{60}^+. However, as the *m/z* ratios of Mg and the one of six He atoms coincide, the C_{60}^+ photofragment spectrum resulting from $C_{60}MgHe_2^+$ fragmentation overlaps again with the spectrum of helium-tagged C_{60}^+, complicating the evaluation. We are not able to observe the tentative dissociation into neutral C_{60} and Mg^+ as we are limited in our time-of-flight mass spectrometer (TOF-MS) when it comes to detecting ions with a small *m/z* ratio.

All absorption spectra of the cationic C_{60} analogs shown in Figure 5 feature a broad absorption in the visible range. The $C_{60}Mg^+$ spectrum additionally shows a rise above 24,000 cm^{-1}. Given that this range was remeasured multiple times and no comparable rise appears in other spectra, we assume that the feature is real. No distinct peaks that could be assigned to DIBs were observed. In contrast to what was expected, the $C_{60}D^+$ ions did not show narrower absorption features than the $C_{60}H^+$ ions, indicating that tunneling of the hydrogen alone cannot explain why the absorption features remain unresolved. The large fluctuations in the $C_{60}D^+$ and especially the $C_{60}H^+$ spectrum are due to low precursor signals and due to the subtraction of the $^{12}C_{58}$ $^{13}C_2^+$ and $^{12}C_{59}$ $^{13}C^+$ isotopes' signal, respectively, which is also prone to uncertainties due to the Poisson statistics of ion counting. The increase in fluctuation toward lower wavenumbers is due to a decrease in the laser power.

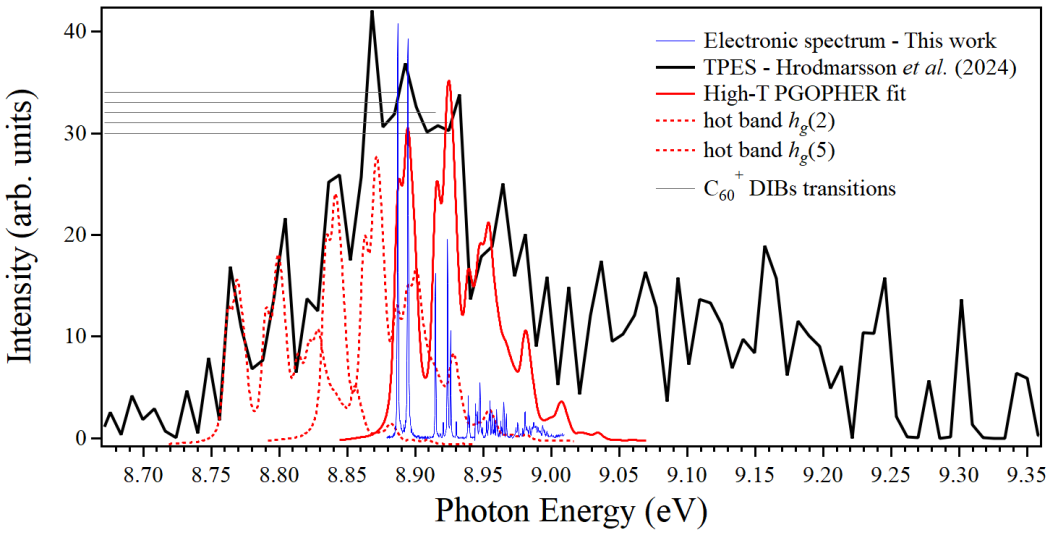

Figure 4. Gas-phase action spectrum of C_{60}^+ (blue) and TPES of H. R. Hrodmarsson et al. (2024, black). The broadened PGOPHER fit from Figure 3 at 900 K is shown in red. The red dashed lines show the same fit only shifted to the red by the Raman-active $h_g(2)$ and $h_g(5)$ vibrational energies. The uncertainty in the TPES intensity is on the order of 5%–10%.

Table 4
Electronic State Energies and Oscillator Strengths f in C_{60}^+ as Calculated Using Quantum-Chemical Methods[a]

State	Energy[b] (cm^{-1})	f [b]	Energy[c] (cm^{-1})	f [c]	Energy[d] (cm^{-1})	f [d]
$^2A_{1u}$	0	…	0	…	0	…
$^2E_{2u}$	2145	0	2442	0	1738	0
$^2E_{1u}$	2191	0	2525	0	1721	0
$^2E_{1g}$	10,705	0.0457	9024	0.0509	11,376	"Bright"
$^2E_{2g}$	13,469	0	13,248	0	12,467	0
$^2A_{1g}$	14,104	0	14,517	0	…	…
$^2E_{2g}$	14,118	0	14,924	0	12,647	0
$^2E_{1g}$	14,421	0.0001	15,366	0.0012	12,744	"Bright"

Notes.
[a] One E_{2u} state at 13,819 cm^{-1} (TD-BMK/6-31+G*//BP86-D3/def2SVP) or rather 8795 cm^{-1} (TD-BHandHLYP/6-31+G*//BP86-D3/def2SVP) with $f = 0$ is not listed due to heavy spin contamination: The multiplicity is calculated as 3.46, making the state rather a quartet than a doublet.
[b] This work: TD-BMK/6-31+G*//BP86-D3/def2SVP level of theory.
[c] This work: TD-BHandHLYP/6-31+G*//BP86-D3/def2SVP level of theory.
[d] A. O. Lykhin et al. (2018): TD-B3LYP/def2-TZVP//TD-B3LYP/def2-TZVP.

To rationalize our observations, we modeled the C_{60}^+, $C_{60}H^+$, and $C_{60}Mg^+$ ions using quantum-chemical calculations as shown in Figure 2. The high symmetry of C_{60}^+ is reduced to C_s upon adsorption of a hydrogen atom, with the C–H bond length calculated as 1.12 Å. We performed CHELPG, Merz–Kollman, natural bond orbital (NBO), and Mulliken charge analysis, and for $C_{60}Mg^+$ also NBO and Mulliken spin density analysis using different quantum-chemical methods (see Appendix F). All in all, the different methods predict a charge on the H atom in $C_{60}H^+$ which is around zero or slightly positive. Thus, the positive charge will be located entirely or almost entirely on the C_{60} unit, as also stated earlier by H. W. Kroto & M. Jura (1992). This is consistent with the large difference in ionization potentials between C_{60} (7.598eV; H. R. Hrodmarsson et al. 2024) and H (13.606 eV). The formed covalent bond explains the high stability of the system against dissociation into C_{60}^+ and H (2.59 eV). Several electronic transitions are predicted to participate in the broad band observed in the experiment; see Figure 5(e). As expected, the orbitals taking part in the most intense excitations are broadly delocalized over the fullerene molecule, not showing a pronounced charge transfer character between the H atom and the C_{60} cage, which follows from natural transition orbital (NTO) analysis (see Figure E2 in Appendix E).

For $C_{60}Mg^+$, a structure with Mg in contact with a carbon atom in C_s symmetry is predicted to be the most stable one, with a Mg···C separation of 2.38 Å, being stabilized by 1.18 eV against dissociation into C_{60}^+ and Mg. An alternative minimum with a magnesium atom above a five-membered ring is less stable by 0.07 eV (see Appendix D). Charge analysis predicts a charge between 0.3 e and 0.9 e on the Mg atom (see Appendix F). NTO analysis confirms that the most intense excitations in $C_{60}Mg^+$ seen in Figure 5(g) exhibit at least some charge transfer character, supporting the pronounced role of magnesium (see Figure E2 in Appendix E). Interestingly, the NTOs show that the magnesium 3s orbital is involved in orbitals with both alpha and beta spin orientation (i.e., as donor and acceptor) for the bright transitions. However, one has to be careful when interpreting density functional theory (DFT) results on such an extended system within a relatively small basis set, and active participation of Mg on the excitations is thus tentative. The width of the spectrum can again be explained by several contributing transitions as well as a somewhat delocalized position of the magnesium cation on the fullerene surface due to low-frequency vibrations.

This rather balanced charge distribution between Mg and the C_{60} cage is consistent with the fact that the ionization potential of C_{60} (7.598 eV; H. R. Hrodmarsson et al. 2024) is very similar to that of Mg (7.646 eV; V. Kaufman & W. C. Martin 1991). Overall, our calculations suggest that the charge on the C_{60} cage decreases from C_{60}^+ ($q = e$) to $C_{60}H^+$ ($q \approx 0.6$ e–1.1 e) to $C_{60}Mg^+$ ($q \approx 0.1$ e–0.7 e) to neutral C_{60} ($q = 0$). This qualitative trend is consistent with the one derived from ionization potentials increasing from 7.598 eV for C_{60} to 7.646 eV for Mg and 13.606 eV for H. Interestingly, the experimentally measured spectra shown in Figure 5 show a

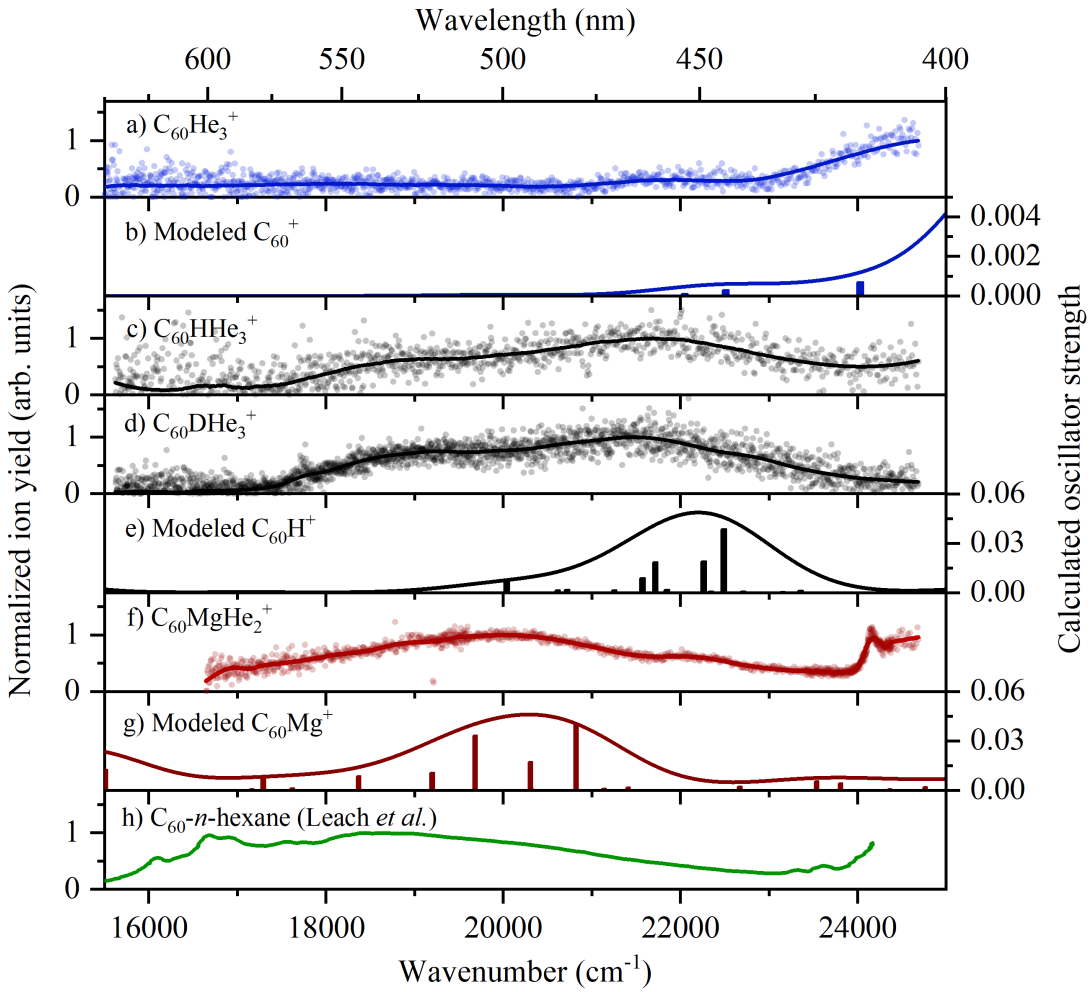

Figure 5. Experimental gas-phase absorption spectra of (a) $C_{60}He_3^+$, (c) $C_{60}HHe_3^+$, (d) $C_{60}DHe_3^+$, and (f) $C_{60}MgHe_2^+$ obtained by measuring the yield of the photofragment (a) C_{60}^+ ($m/z = 720$), (c) $C_{60}H^+$ ($m/z = 721$), (d) $C_{60}D^+$ ($m/z = 722$), and (f) $C_{60}Mg^+$ ($m/z = 744$), respectively. Panels (b), (e), and (g) show the modeled spectra of C_{60}^+, $C_{60}H^+$, and $C_{60}Mg^+$ as obtained at the TD-BMK/6-31+G*//BP86-D3/def2SVP level of theory. The spectral shape was modeled through empirical Gaussian broadening with a FWHM of 0.2 eV (≈1610 cm^{-1}). The spectra were shifted by 2000 cm^{-1} to lower energies, accounting for zero-point energy effects. Panel (h) shows the room-temperature absorption spectrum of neutral C_{60} in an *n*-hexane solution measured by S. Leach et al. (1992).

consistent redshift within the same sequence of molecular systems. It should be noted here that the spectrum of neutral C_{60} is recorded in an *n*-hexane solution which supposedly will entail a broadening and shifting of the absorptions compared to gas-phase C_{60}. The calculated spectra show qualitatively the same redshift from C_{60}^+ to $C_{60}H^+$ to $C_{60}Mg^+$ as the experimental ones. The calculated spectrum of neutral C_{60} does not have any allowed transitions, as mentioned above. These three trends which are all consistent with each other suggest that the decreasing charge localization on the C_{60} unit when following this sequence of ions might tentatively explain the redshift in the spectra. However, calculating charge distribution is neither trivial nor well defined for such a complicated system, making the explanation rather vague.

3. Conclusion

We have measured the gas-phase electronic spectra of C_{60}^+, $C_{60}H_2O^+$, $C_{60}H^+$, $C_{60}D^+$, and $C_{60}Mg^+$ by employing a helium-tagging messenger spectroscopy setup. The distinct near-IR absorption bands found in the C_{60}^+ spectrum match with the bands reported earlier by E. K. Campbell et al. (2016b). We have also made several assignments in the C_{60}^+ spectrum based on the pseudo-JT formalism proposed by A. O. Lykhin et al. (2018). We suggest the weakest peaks in the spectrum correspond to excitations from the ground state to ^2E vibrational manifolds, but these cannot be definitely assigned. The energetic sequence by which the different ^2E states should appear can be reproduced semi-quantitatively by our theoretical methods, so these assignments can only be made tentatively for the time being. Water attachment to the C_{60}^+ cation yields absorption features in the spectral vicinity of the C_{60}^+ DIB transition bands, confirming that water is acting mostly as a spectator. In the measured spectra of $C_{60}H^+$, $C_{60}D^+$, and $C_{60}Mg^+$, a broad absorption is observed between 17,000 cm^{-1} and 25,000 cm^{-1}. This absorption is redshifted from C_{60}^+ over $C_{60}H^+$ to $C_{60}Mg^+$ both in the experiment and in the calculations, which could be due to the decreasing charge localization on the C_{60} unit. Even though we did not observe any narrow absorption bands in the presented $C_{60}H^+$, $C_{60}D^+$, and $C_{60}Mg^+$ spectra that can be assigned to known DIB transitions, we provide here the first laboratory electronic spectra of these ionic species, which probably belong to the most abundant C_{60}^+ analogs in the ISM.

Acknowledgments

We sincerely thank Paul Scheier for his support and input. The computational results presented have been achieved using the high-performance computing infrastructure LEO of the University of Innsbruck. This research was funded in whole or in part by the Austrian Science Fund (FWF; 10.55776/V1035, 10.55776/P34563, 10.55776/P35013, 10.55776/W1259, 10.55776/I6221). G.S. acknowledges receipt of a DOC Fellowship of the Austrian Academy of Sciences. This article is based upon work from COST Action CA21126 – Carbon molecular nanostructures in space (NanoSpace), supported by COST (European Cooperation in Science and Technology). AI was used for minor assistance in terms of language and readability.

Appendix A
Experimental Methods

A more detailed description of the employed setup can be found in S. Bergmeister et al. (2023), whereas the basics of the experimental procedure are explained in the following. Superfluid HNDs were produced in a supersonic expansion of helium gas at ≈8.5 K and ≈22 bar through a 5 μm-sized nozzle into vacuum. The HNDs were multiply, positively charged by the impact of an electron beam (≈40 eV; F. Laimer et al. 2019) and guided through a differentially pumped chamber equipped with an electrostatic sector. When protonated, deuterated, or hydrated species were studied, gas-phase H_2, D_2, or H_2O was introduced into the sector chamber and picked up by the charged HNDs, respectively. Inside the HNDs, the dopants could be charged via charge transfer or Penning ionization from charged or excited helium, creating H_3^+, D_3^+ (L. Tiefenthaler et al. 2020), or H_2O^+ ions. After the electrostatic sector, the HNDs entered the pickup chamber, which was equipped with an ohmically heated oven. Passing the oven, the HNDs were doped with C_{60}. Protonated and deuterated C_{60} species formed upon the transfer of H^+ or D^+ from the H_3^+ or D_3^+ ions onto the C_{60} molecule, respectively (L. Tiefenthaler et al. 2020). Agglomeration of additional dopants around the charge sites eventually yielded $(C_{60})_i(H_2O)_j^+$, $(C_{60})_iH(H_2)_k^+$, or $(C_{60})_iD(D_2)_l^+$ cluster ions embedded in the HND. The cluster size (i, j, k, and l) could be adjusted by regulating the dopant pressure with the oven power and the gas-inlet system. For the measurements with $C_{60}H^+$ and $C_{60}D^+$, the pressure of the introduced hydrogen and deuterium was tuned so that k and l were essentially 0. In the case of $C_{60}Mg^+$, magnesium was evaporated in the same oven as C_{60} which proved possible as magnesium and C_{60} have similar vapor pressures. The size of the formed clusters, $(C_{60})_iMg_m^+$, was adjusted via the oven power setting to obtain primarily $C_{60}Mg^+$ monomers. Behind the pickup chamber, the doped HNDs were guided through a chamber filled with room-temperature helium gas. Collisions with the room-temperature helium gas led to evaporation of the HNDs, and dopant ions—tagged with only a few or no helium atoms—were liberated from the HNDs. The number of attached helium atoms could be controlled via the pressure of the helium gas. The liberated ions then reached a quadrupole mass filter, which allowed us to select specific ions based on their mass-to-charge ratio. The beam of selected ions was irradiated with a pulsed laser (EKSPLA NT242 or EKSPLA NT262). The line width of the EKSPLA NT262 laser is $<3\,cm^{-1}$ for wavelengths >480 nm and $<5\,cm^{-1}$ for wavelengths <480 nm. The line width of the EKSPLA NT242 laser is $<5\,cm^{-1}$ in the measured range. The measurements of C_{60}^+, $C_{60}H^+$, $C_{60}D^+$, and cold $C_{60}(H_2O)_j^+$ were conducted with the EKSPLA NT262 laser, whereas the $C_{60}Mg^+$ and warm $C_{60}H_2O^+$ spectra were measured with the EKSPLA NT242 laser. The ions—including the photofragments and the precursor ions—were detected in a TOF-MS with a repetition rate of 10 kHz. Concurrently, the laser was operated with a rate of 1 kHz (EKSPLA NT242) or 5 kHz (EKSPLA NT262). Thus, mass spectra with and without the influence of the laser were obtained virtually synchronously. The absorption spectra were gained by measuring the (normalized) photofragment yield as a function of the laser frequency. The normalized photofragment yield Y at a specific laser frequency was calculated as follows:

$$Y = (Y_{\text{Fragment}} - Y_{\text{Background}})/(Y_{\text{Precursor}} \times N_{\text{Photons}}). \quad \text{(A1)}$$

Here, Y_{Fragment} and $Y_{\text{Background}}$ denote the counts at the m/z of the photofragment in the mass spectra with and without laser irradiation, respectively. $Y_{\text{Precursor}}$ are the counts of the precursor ion in the mass spectra without laser irradiation, and N_{Photons} denotes the number of photons, obtained by measuring the laser power. The laser wavelength was calibrated with a wavemeter (SHR High-resolution Wide-range Spectrometer). The wavelength data in this contribution correspond to the wavelength in air. To convert the data into wavenumbers, a refractive index of 1.00027 was assumed.

Appendix B
Evaluation of the $C_{60}H^+$ and $C_{60}D^+$ Spectra

The evaluation procedure is explained for $C_{60}H^+$. The $C_{60}D^+$ spectrum was obtained analogously. As mentioned in Section 2, the m/z ratio of the desired $C_{60}HHe_3^+$ ions overlaps with the m/z ratio of the unprotonated isotope $^{12}C_{59}\,^{13}CHe_3^+$ (m/z = 733). Upon photon absorption, both the unprotonated isotope and the protonated ion lose the attached helium atoms and dissociate into the same m/z ratio, namely m/z = 721. To obtain purely the $C_{60}H^+$ yield ($Y_{C_{60}H^+}$), we had to subtract the contribution of the unprotonated C_{60}^+ isotope ($Y_{^{12}C_{59}\,^{13}C^+}$) from the measured m/z = 721 photofragment yield ($Y_{m/z\,=\,721}$) for each photon frequency: $Y_{C_{60}H^+} = Y_{m/z=721} - Y_{^{12}C_{59}\,^{13}C^+}$. In order to calculate $Y_{^{12}C_{59}\,^{13}C^+}$, the yield of the photofragment $^{12}C_{60}^+$ ($Y_{m/z\,=\,720}$) emerging from the photofragmentation of $^{12}C_{60}He_3^+$ was recorded. Thus, $^{12}C_{60}He_3^+$, with its yield $Y_{m/z\,=\,732}$, was also allowed to pass the quadrupole. Then, $Y_{^{12}C_{59}\,^{13}C^+}$ is calculated as $a \times Y_{m/z\,=\,720}$, with

$$a \approx \underbrace{\frac{\overbrace{0.649 \times \tilde{Y}_{m/z=732}}^{(2)}}{\tilde{Y}_{m/z=733}}}_{(1)} \times Y_{m/z=733}/Y_{m/z=732}. \quad \text{(B1)}$$

Here, $Y_{m/z\,=\,732,733}$ denotes the precursor ion yield at m/z = 732 and 733, respectively. To account for the fact that the selection with the quadrupole mass filter alters the peak ratio, a separate mass spectrum without quadrupole mass selection was recorded immediately before the absorption spectrum. $\tilde{Y}_{m/z=732,733}$ designates the ion yield at m/z = 732 and 733 from this mass spectrum, respectively. 0.649 is the isotope ratio $^{12}C_{59}^{13}C/^{12}C_{60}$. The term (1) equals the ratio of the $^{12}C_{59}{}^{13}CHe_3^+$ yield to the whole $\tilde{Y}_{m/z=733}$. Thus, (2) equals

the yield of $^{12}C_{59}$ $^{13}CHe_3^+$ at $m/z = 733$ in the spectroscopy measurement. Accordingly, the factor a corresponds to the ion yield ratio of the precursor $^{12}C_{59}$ $^{13}CHe_3^+$ to the precursor $^{12}C_{60}He_3^+$. Multiplying the factor a with the $Y_{m/z\,=\,720}$ signal yields the signal of $Y_{^{12}C_{59}\,^{13}C^+}$ in $Y_{m/z\,=\,721}$. Subtraction of $Y_{^{12}C_{59}\,^{13}C^+}$ from $Y_{m/z\,=\,721}$ then yields $Y_{C_{60}H^+}$.

Appendix C
Experimental Absorption Spectra of C_{60}-water Clusters

Figure C1 shows the helium-tagging spectra of $C_{60}(H_2O)^+$ ($j = 1$–4).

Appendix D
Theory

For structure optimization and calculation of electronic excitations, we followed a methodology which was already successfully applied to C_{120}^- (M. Kappe et al. 2023). Namely, optimization of $C_{60}(H_2O)^+$, C_{60}^+, $C_{60}H^+$, and $C_{60}Mg^+$ ions was performed using the BP86 functional within DFT along with the def2SVP basis set and D3 dispersion correction (S. Grimme et al. 2010), subsequently performing vibrational analysis within harmonic approximation to confirm the local minimum character of all structures. Electronic states were calculated through the time-dependent DFT approach (or

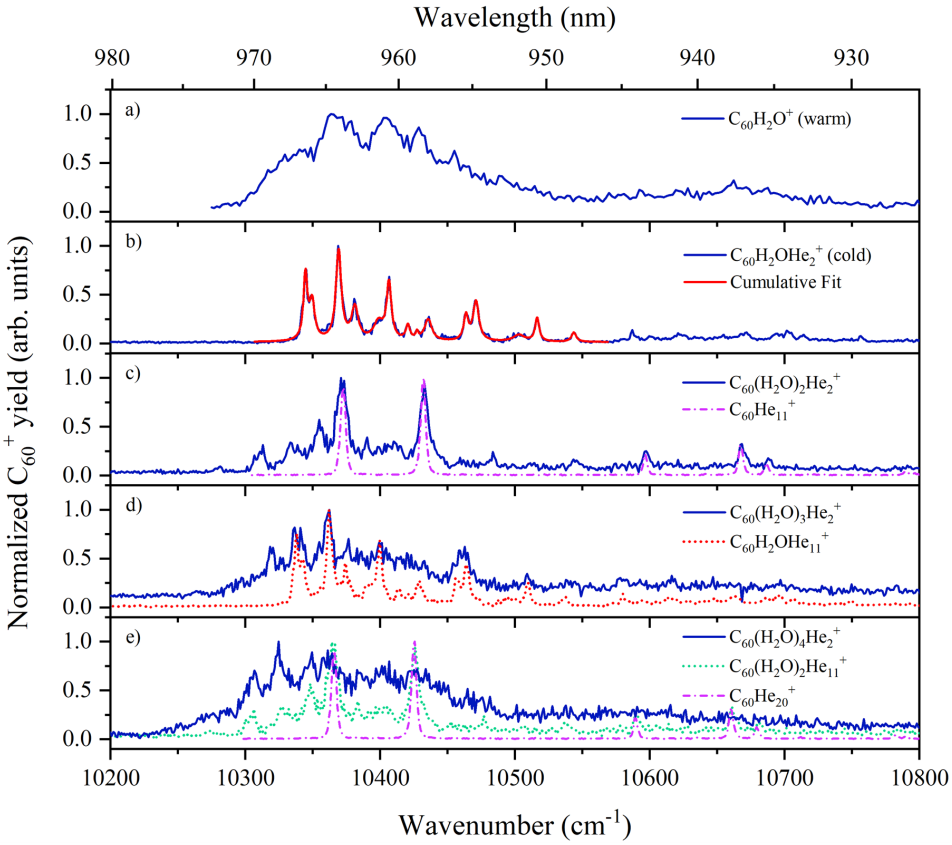

Figure C1. Experimental absorption spectra of (a) $C_{60}H_2O^+$ and of (b)–(e) $C_{60}(H_2O)_jHe_2^+$ ($j = 1$–4) obtained by recording the C_{60}^+ photofragment yield. The $C_{60}H_2OHe_2^+$ spectrum in (b) is fitted with cumulative Lorentzian functions (red line). Their central positions and relative cross sections are given in Table 2 in the manuscript. The photofragment spectra of $C_{60}(H_2O)_jHe_2^+$ ($j = 2$–4) in (c)–(e) overlap with the photofragment spectra of helium-tagged C_{60}^+ (purple), $C_{60}H_2O^+$ (red dots), or $C_{60}(H_2O)_2^+$ (cyan) due to the fact that the mass of nine He atoms is only 0.0023u less than the mass of a water dimer. This minuscule mass difference cannot be resolved with the quadrupole mass filter. Hence, the selected peaks at the m/z of $C_{60}(H_2O)_2He_2^+$ contain contributions from $C_{60}He_{11}^+$ (purple); the selected peaks at the m/z of $C_{60}(H_2O)_3He_2^+$ contain contributions from $C_{60}H_2OHe_{11}^+$ (red dots); and the selected peaks at the m/z of $C_{60}(H_2O)_4He_2^+$ contain contributions from $C_{60}(H_2O)_2He_{11}^+$(cyan) and $C_{60}He_{20}^+$ (purple). The purple lines depict the measured absorption spectra of $C_{60}He_2^+$ to which a wavelength shift of 0.07 nm per additional helium atom was applied to account for the effect of the attached 11/20 helium atoms, respectively. The red and cyan lines depict the measured spectra of $C_{60}H_2OHe_2^+$ and $C_{60}(H_2O)_2He_2^+$, respectively, including a shift of 0.07 nm per additional helium atom to account for the effect of the in total 11 attached helium atoms. As all these helium-tagged or hydrated ions dissociate into bare C_{60}^+ upon photon absorption in this spectral range, their absorption spectra cannot be distinguished from each other. However, even though the spectra are partly corrupted, a slight redshift of the absorption bump for complexes with more water molecules attached can be perceived.

Table D1

Energy E, Oscillator Strength f, and Expectation Value $\langle \hat{S}^2 \rangle$ for Calculated Allowed Transitions in C_{60}^+ as Obtained at the TD-BMK/6-31+G*//BP86/def2SVP Level

E (eV)	f	$\langle \hat{S}^2 \rangle$
1.3273	0.0457	0.789
1.3273	0.0457	0.789
1.7880	0.0001	0.784
1.7880	0.0001	0.784
2.9816	0.0001	2.746
3.0392	0.0003	2.719
3.0392	0.0003	2.719
3.2271	0.0007	1.820
3.3589	0.0007	0.800
3.3590	0.0007	0.800
3.4581	0.0074	1.110
3.5802	0.0005	2.645
3.6290	0.0068	0.819
3.6290	0.0068	0.819
3.6723	0.0002	2.665
3.6723	0.0002	2.665
3.7681	0.0004	0.818

TDDFT) with BMK, CAM-B3LYP, and BHandHLYP functionals and the 6-31+G* basis set. All functionals provided rather similar spectra. Note that there is a high spin contamination in low-intensity transitions for radical species shown in Figure 5 whose energy and intensity should be thus interpreted with caution. Table D1 (C_{60}^+) and Table D2 ($C_{60}H^+$ and $C_{60}Mg^+$, published in its entirety in machine-readable format) show the calculated energy E, oscillator strength f, and expectation value $\langle \hat{S}^2 \rangle$ for calculated allowed transitions. To model the spectral shape, we employed Gaussian broadening with an empirical FWHM chosen as 0.2 eV. To obtain more reliable reaction energies, we performed reoptimizations on the BP86-D3/aug-cc-pVDZ level of theory. A comparison to reaction energies from BLYP-D3/aug-cc-pVDZ, PBE-D3/aug-cc-pVDZ, BP86-D3/def2SVP, and BP86-D3/aug-cc-pVDZ//BP86-D3/def2SVP is given in Table D3. The calculations were performed in the Gaussian software (M. J. Frisch et al. 2016); electron transitions were analyzed using the NTO scheme (R. L. Martin 2003).

Table D2

Energy E, Oscillator Strength f, and Expectation Value $\langle \hat{S}^2 \rangle$ for Calculated Allowed Transitions in $C_{60}H^+$ and $C_{60}Mg^+$ as Obtained with Various Functionals with the 6-31+G* Basis Set in the Structure Obtained at the BP86-D3/def2SVP Level

System	BHandHLYP			CAM-B3LYP			BMK		
	E (eV)	f	$\langle \hat{S}^2 \rangle$	E (eV)	f	$\langle \hat{S}^2 \rangle$	E (eV)	f	$\langle \hat{S}^2 \rangle$
$C_{60}H^+$	1.4335	0.0035	0.0	1.441	0.0039	0.0	1.3304	0.0026	0.0
$C_{60}H^+$	1.5404	0.0002	0.0	1.5662	0.0005	0.0	1.4037	0.0001	0.0
$C_{60}H^+$	1.5546	0.0073	0.0	1.5754	0.0077	0.0	1.4301	0.0062	0.0
$C_{60}H^+$	1.5738	0.0036	0.0	1.5966	0.004	0.0	1.4459	0.0029	0.0
…	…	…	…	…	…	…	…	…	…
$C_{60}Mg^+$	3.7196	0.0022	1.913	3.7716	0.0025	1.862	3.7308	0.0008	1.276
$C_{60}Mg^+$	3.7241	0.0026	1.617	3.8059	0.0145	1.345	…	…	…
$C_{60}Mg^+$	3.7474	0.001	2.646	3.8151	0.0004	1.8	…	…	…
$C_{60}Mg^+$	3.7497	0.0019	1.759	3.8359	0.0005	2.26	…	…	…
$C_{60}Mg^+$	3.7844	0.0011	1.363	3.8494	0.0003	2.173	…	…	…

(This table is available in its entirety in machine-readable form in the online article.)

Table D3

Reaction Energies in eV for Reactions $C_{60}^+ + M \rightarrow C_{60}M^+$, M = {H, Mg, H_2O} for Different Levels of Theory

Reaction	BP86-D3/aug-cc-pVDZ	BLYP-D3/aug-cc-pVDZ	PBE-D3/aug-cc-pVDZ	BP86-D3/def2SVP	BP86-D3/aug-cc-pVDZ//BP86-D3/def2SVP
$C_{60}^+ + H \rightarrow C_{60}H^+$	−2.59	−2.47	−2.46	−2.64	−2.57
$C_{60}^+ + Mg \rightarrow C_{60}Mg^+$ (iso1)	−1.18	−0.95	−1.14	−1.30	−1.23
$C_{60}^+ + Mg \rightarrow C_{60}Mg^+$ (iso2)	−1.11	…	−1.14	−1.22	−1.15
$C_{60}^+ + H_2O \rightarrow C_{60}H_2O^+$	−0.11	−0.13	−0.12	−0.29	−0.06

Note. At the BLYP-D3/aug-cc-pVDZ level of theory, iso2 of $C_{60}Mg^+$ is a transition state and converges into iso1 upon a push along the respective eigenvector.

Appendix E
Electronic Transition Calculations

Figure E1 illustrates the electronic transition energy as calculated in this work. Figure E2 depicts the electronic transitions in $C_{60}H^+$ and $C_{60}Mg^+$ contributing to the modeled spectra shown in Figure 5.

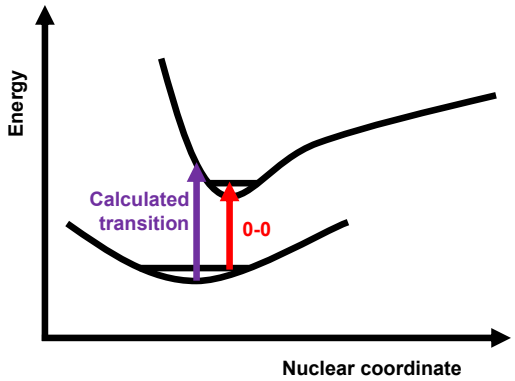

Figure E1. The purple arrow shows the electronic transition energy as calculated in this work. The red arrow shows the 0–0 transition energy. Note that this scheme only shows the ground electronic state and one electronically excited state.

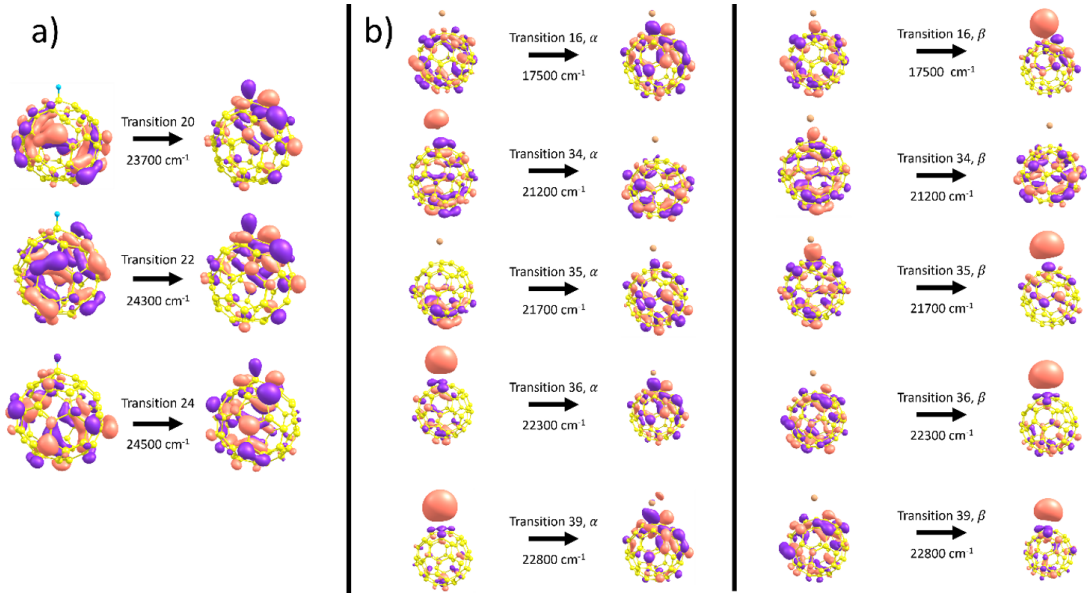

Figure E2. The most important electronic transitions involved in (a) $C_{60}H^+$ and (b) $C_{60}Mg^+$ as shown in Figure 5 of the manuscript, calculated at the TD-BMK/6-31+G* level of theory. Orange and purple are the positive and negative phase of the wave function, respectively. The energy and number of transitions are also given. In the case of $C_{60}Mg^+$, alpha and beta spin orbitals are shown. When comparing these transitions to the ones shown in Figure 5, note that in Figure 5 the modeled spectrum is shifted by 2000 cm^{-1} to lower energies, so that for example the bundle of transitions in $C_{60}H^+$ at around 22,000 cm^{-1} in Figure 5 corresponds to transitions at around 24,000 cm^{-1} in this figure.

Appendix F
Charge Analysis

In the case of $C_{60}H^+$, Merz–Kollman charge analysis predicts a charge slightly above zero for all quantum-chemical methods investigated here, whereas CHELPG charge analysis consistently gives values slightly below zero. Charge analysis via NBOs predicts a charge of around 0.35 e on the H atom. For these three charge analysis methods, the quantum-chemical method only has a minor influence. The maximum difference is 0.13 e in the case of Merz–Kollman, 0.12 e for CHELPG, and 0.03 e for NBO analysis. Overall, this suggests that the charge on the H atom in $C_{60}H^+$ is around zero or slightly positive. The average of all values predicted with Mulliken charge analysis (0.12 e) is consistent with this. However, the individual levels of theory lead to significantly deviating Mulliken charges between –0.27 e for BLYP-D3/aug-cc-pVDZ and +0.32 e for PBE-D3/6-31+G*//BP86-D3/def2SVP. This can be explained by the well-known basis set dependence of Mulliken charges. In the case of $C_{60}Mg^+$, Merz–Kollman charge analysis and CHELPG charge analysis

Table F1
Charges (in Units of e) and Spin Density on the H and the Mg Atoms in $C_{60}H^+$ and $C_{60}Mg^+$, Respectively, as Calculated with Different Quantum Chemical Methods and Charge Analysis Methods, along with Their Arithmetic Average

	$C_{60}H^+$				$C_{60}Mg^+$					
	MK	CHELPG	NBO	Mulliken	MK	CHELPG	NBO	Mulliken	Mulliken SD	NBO SD
BMK/6-31+g*//BP86-D3/def2SVP	0.13	−0.06	0.37	0.31	0.48	0.38	0.96	0.68	0.85	0.89
PBE-D3/6-31+g*//BP86-D3/def2SVP	0.10	−0.08	0.36	0.32	0.44	0.34	0.92	0.57	0.84	0.83
BLYP-D3/6-31+g*//BP86-D3/def2SVP	0.03	−0.16	0.34	0.29	0.38	0.27	0.89	0.56	0.81	0.81
PBE-D3/aug-cc-pVDZ	0.10	−0.10	0.35	−0.04	0.45	0.33	0.94	0.36	0.84	0.83
BLYP-D3/aug-cc-pVDZ	0.00	−0.18	0.33	−0.27	0.39	0.28	0.89	0.30	0.81	0.81
Average	0.07	−0.12	0.35	0.12	0.43	0.32	0.93	0.49	0.83	0.83

Note. "MK" stands for Merz–Kollman. "SD" stands for spin density. For $C_{60}Mg^+$, the Mulliken spin density and the spin density from natural bond orbital (NBO) analysis are also given (last two columns).

predict values of around +0.3 e to +0.4 e on the Mg atom, again with only little dependence on the quantum-mechanical method used (maximum difference is 0.10 e in the case of Merz–Kollman and 0.11 e for CHELPG). NBO analysis gives a much higher charge on the Mg atom, namely around 0.9 e. As $C_{60}Mg^+$ is an open-shell system, we have also calculated the Mulliken spin density on Mg in this system. Mulliken spin densities and spin densities from NBO analysis are given as around 0.8, indicating that the Mg atom has almost fully donated its beta electron, translating into a charge of around 0.8 e on the Mg atom. Mulliken charges are somewhere in between, again with large deviations between the different quantum-chemical methods. All charge calculations predict a higher charge on Mg in $C_{60}Mg^+$ than on H in $C_{60}H^+$. However, there is some discrepancy among the different methods regarding the exact value. For H, the charge seems to be somewhere between –0.1 e and 0.4 e; for Mg, the charge seems to be somewhere between 0.3 e and 0.9 e. It should be noted here that even though these differences appear quite substantial, the differences are not that surprising, because there is no unique definition about how to assign partial charges to the different atoms in a molecular system. Table F1 shows the charge analysis for $C_{60}H^+$ and $C_{60}Mg^+$, respectively.

Appendix G
Cartesian Coordinates and Electronic Energies

Cartesian coordinates and electronic energies E including zero-point correction of all systems optimized at the BP86-D3/def2SVP, BP86-D3/aug-cc-pVDZ, and BLYP-D3/aug-cc-pVDZ levels of theory are published in Table G1 and given in their entirety in machine-readable format.

Table G1
Cartesian Coordinates and Electronic Energies E Including Zero-point Correction Optimized at the BP86-D3/def2SVP, BP86-D3/aug-cc-pVDZ, and BLYP-D3/aug-cc-pVDZ Levels of Theory

Level	System	E (E_h)	Atom	X (Å)	Y (Å)	Z (Å)
BP86-D3/def2SVP	C_{60}^+	−2284.144595	C	0.723156	3.425701	0.603932
…	…	…	…	…	…	…
BP86-D3/def2SVP	$C_{60}H^+$	−2284.740898	C	−1.986841	−1.422673	2.612670
…	…	…	…	…	…	…
…	…	…	…	…	…	…
…	…	…	…	…	…	…
…	…	…	…	…	…	…
BLYP-D3/aug-cc-pVDZ	H_2O	−76.406849	O	0.0	0.0	0.119991
…	…	…	…	…	…	…
BLYP-D3/aug-cc-pVDZ	H	−0.49701	H	0.0	0.0	0.0
BLYP-D3/aug-cc-pVDZ	Mg	−200.077115	Mg	0.0	0.0	0.0

(This table is available in its entirety in machine-readable form in the online article.)

ORCID iDs

Lisa Ganner https://orcid.org/0000-0002-0344-565X
Gabriel Schöpfer https://orcid.org/0000-0001-5657-2671
Alexander Ebenbichler https://orcid.org/0000-0002-6994-1007
Stefan Bergmeister https://orcid.org/0000-0003-0848-3038
Milan Ončák https://orcid.org/0000-0002-4801-3068
Helgi Rafn Hrodmarsson https://orcid.org/0000-0002-9613-5684
Elisabeth Gruber https://orcid.org/0000-0002-1195-3638

References

Abbink, D., Foing, B., & Ehrenfreund, P. 2024, A&A, 684, A165
Albertini, S., Gruber, E., Zappa, F., et al. 2021, MSRv, 41, 529
Asplund, M., Amarsi, A. M., & Grevesse, N. 2021, A&A, 653, A141
Álvaro Galué, H., Oomens, J., Buma, W. J., & Redlich, B. 2016, NatCo, 7, 12633
Bergmeister, S., Ganner, L., Locher, J., et al. 2023, RScI, 94, 055105
Brieva, A. C., Gredel, R., Jäger, C., Huisken, F., & Henning, T. 2016, ApJ, 826, 122
Cami, J., Bernard-Salas, J., Peeters, E., & Malek, S. E. 2010, Sci, 329, 1180
Campbell, E. K., Holz, M., Gerlich, D., & Maier, J. P. 2015, Natur, 523, 322
Campbell, E. K., Holz, M., & Maier, J. P. 2016a, ApJL, 826, L4
Campbell, E. K., Holz, M., Maier, J. P., et al. 2016b, ApJ, 822, 17
Campbell, E. K., & Maier, J. P. 2018, ApJ, 858
Cernicharo, J., Cabezas, C., Pardo, J. R., et al. 2023, A&A, 672, L13
Denifl, S., Zappa, F., Mähr, I., et al. 2009, AngCh, 121, 9102
Díaz-Luis, J. J., García-Hernández, D. A., Manchado, A., & Cataldo, F. 2016, A&A, 589, A5
Fan, H., Hobbs, L. M., Dahlstrom, J. A., et al. 2019, ApJ, 878, 151
Finazzi, L., Esposito, V. J., Palotás, J., et al. 2024, ApJ, 971, 168
Foing, B. H., & Ehrenfreund, P. 1994, Natur, 369, 296
Frisch, M. J., Trucks, G. W., Schlegel, H. B., et al., 2016 Gaussian 16, Revision A.03, Wallingford, CT: Gaussian Inc.
Fulara, J., Jakobi, M., & Maier, J. P. 1993, CPL, 211, 227
Grimme, S., Antony, J., Ehrlich, S., & Krieg, H. 2010, JChPh, 132, 154104
Hansen, K., & Echt, O. 1997, PhRvL, 78, 2337
Hardy, F.-X. 2016, PhD thesis, Univ. Basel
Hernández-Rojas, J., Calvo, F., Rabilloud, F., Bretón, J., & Gomez Llorente, J. M. 2010, JPCA, 114, 7267
Hou, G.-L., Lushchikova, O. V., Bakker, J. M., et al. 2023, ApJ, 952, 13
Hrodmarsson, H. R., Garcia, G. A., Linnartz, H., & Nahon, L. 2020, PCCP, 22, 13880
Hrodmarsson, H. R., Rapacioli, M., Spiegelman, F., et al. 2024, JChPh, 160, 164314
Kappe, M., Schiller, A., Gruber, E., et al. 2023, JChPh, 159, 204302
Kaufman, V., & Martin, W. C. 1991, JPCRD, 20, 83
Kroto, H. W., Heath, J. R., O'Brien, S. C., Curl, R. F., & Smalley, R. E. 1985, Natur, 318, 162
Kroto, H. W., & Jura, M. 1992, A&A, 263, 275
Kuhn, M., Renzler, M., Postler, J., et al. 2016, NatCo, 7, 13550
Lacinbala, O., Calvo, F., Falvo, C., et al. 2023, PhRvA, 107, 062808
Laimer, F., Kranabetter, L., Tiefenthaler, L., et al. 2019, PhRvL, 123, 165301
Leach, S., Vervloet, M., Desprès, A., et al. 1992, CP, 160, 451
Linnartz, H., Cami, J., Cordiner, M., et al. 2020, JMoSp, 367, 111243
Lykhin, A. O., Ahmadvand, S., & Varganov, S. A. 2018, JPCL, 10, 115
Manini, N., Dal Corso, A., Fabrizio, M., & Tosatti, E. 2001, PMagB, 81, 793
Martin, R. L. 2003, JChPh, 118, 4775
Muigg, D., Scheier, P., Becker, K., & Märk, T. D. 1996, JPhB, 29, 5193
Nie, T. P., Xiang, F. Y., & Li, A. 2022, MNRAS, 509, 4908
Page, R. H., Larkin, R. J., Shen, Y. R., & Lee, Y. T. 1988, JChPh, 88, 2249
Palotás, J., Martens, J., Berden, G., & Oomens, J. 2020, NatAs, 4, 240
Rademacher, J., Reedy, E. S., Negri, F., et al. 2023, MolPh, 122, e2173507
Roberts, K. R. G., Smith, K. T., & Sarre, P. J. 2012, MNRAS, 421, 3277
Sellgren, K., Werner, M. W., Ingalls, J. G., et al. 2010, ApJL, 722, L54
Tiefenthaler, L., Kollotzek, S., Ellis, A. M., Scheier, P., & Echt, O. 2020, PCCP, 22, 28165
van Dishoeck, E. F., Herbst, E., & Neufeld, D. A. 2013, ChRv, 113, 9043
Walker, G. A. H., Bohlender, D. A., Maier, J. P., & Campbell, E. K. 2015, ApJ, 812, L8
Walker, G. A. H., Campbell, E. K., Maier, J. P., Bohlender, D., & Malo, L. 2016, ApJ, 831, 130
Western, C. M. 2017, JQSRT, 186, 221
Zhang, Y., Sadjadi, S., Hsia, C.-H., & Kwok, S. 2017, ApJ, 845, 76